

Supporting Information for:

Trapped water molecules are essential to structural dynamics and function of a ribozyme

Maria M. Rhodes^{*}, Kamila Reblova[†], Jiří Šponer^{†,‡,§}, Nils G. Walter^{*,§}

^{*}Department of Chemistry, Single Molecule Analysis Group, University of Michigan, 930 N. University Avenue, Ann Arbor, MI 48109-1055. [†]Institute of Biophysics, Academy of Sciences of the Czech Republic, Královopolská 135, 612 65 Brno, Czech Republic. [‡]Institute of Organic Chemistry and Biochemistry, Academy of Sciences of the Czech Republic, Prague.

[§]Correspondence should be addressed to N.G.W., Department of Chemistry, University of Michigan, 930 N. University Avenue, Ann Arbor, MI 48109-1055. Phone: (734) 615-2060, Fax: (734) 647-4865, E-mail: nwalter@umich.edu; or J.S., Institute of Biophysics, Academy of Sciences of the Czech Republic, Královopolská 135, 612 65 Brno, Czech Republic. Phone: +420 5415 17133, Fax: +420 5412 12179, E-mail: sponer@ncbr.chemi.muni.cz.

This PDF file includes:

Supporting Methods
Supporting Table 1 to 5
Supporting Text
Supporting Figs. 4 to 17

Supporting Methods

Solvent-tracking perl scripts. The carnal module of AMBER6.0 and specialized perl scripts were used in the detection and identification of water molecules with nanosecond-timescale residencies. Any individual water molecule contacting any portion of the ribozyme for ≥ 5 ns, whether continuous or not, passed into the second round of selection; typically, 80 to 100 water molecules passed this first selection criterion out of ~ 9000 total solvent molecules. The distances from these selected waters to catalytically important nucleotides and the occupancies of hydrogen bonds with the RNA were calculated using the ptraj module.

Visual inspection of trajectories edited to remove the ~ 8900 bulk water molecules indicated that 20-50% of the water molecules that passed the first selection criterion were resident inside the interdomain cavity of the ribozyme for several nanoseconds. The remaining waters either had been resident in the major groove of domain B and then returned to bulk or had been trapped in the solvation shell of the Mg^{2+} cations. In the second round of water selection, the ~ 70 -90 waters that remained on the exterior of the ribozyme were disregarded. None of the intracavity water molecules described in this paper were located in the first or second solvation shell of a metal cation. To check that all intracavity water molecules had been found in the WT-Mg simulations, coordinate files were generated at half-nanosecond intervals using AMBER's ptraj module; these snapshots contained the two hundred waters closest to the cavity and were visually inspected in VMD. No new interdomain waters were discovered from this final inspection.

B-factors for the four-way junction hairpin ribozyme were averaged by nucleotide across both molecules in the asymmetrical subunit of the crystal structure PDB ID 1M5K, an updated version of PDB ID 1HP6 (1); those labeled as the junctionless hairpin ribozyme are averaged by nucleotide from PDB ID 1ZFR (2).

Hydrogen bond inventories. To obtain a detailed inventory of the direct interdomain RNA-RNA hydrogen bonds, the ptraj module of AMBER-8 was used to track possible hydrogen bonds between bases which participated in known interdomain interactions in the wild-type (WT) hairpin ribozyme. For each simulation, these hydrogen bond distances were tracked from 0 to 100 ps (after equilibration) to obtain an initial inventory of hydrogen bonds and from 9.9 to 10 ns to obtain the remaining inventory after 10 ns of MD simulation. Fractional hydrogen bonds were derived from the fraction of time that the heavy-atom distances of these hydrogen bonds were ≤ 3.1 Å and that the X-H---Y angle was within 60° of linearity.

The inventories of hydrogen bonds of the sixteen waters entering the interdomain cavity during the WT-Mg simulations were taken over 10 ps intervals. Nine waters entered between the purine rings of bases G+1 and A38 as depicted in **Fig. 2e**, with A38 lifting away from G+1 and rolling towards A24 (rotating counterclockwise along A38's glycosidic bond). Five waters passed between the purine rings of G+1 and A38 in a manner slightly altered from figure 5a, in that A38 rolls away from A24 (i.e., rotating clockwise). These fourteen water molecules provide the vaporization data for **Fig. 2f**. The ptraj module of AMBER-8 was used to track any hydrogen bond that an entering water molecule had with another water molecule or an atom belonging to the ribozyme. Perl scripts were used to derive the number of fractional hydrogen bonds over each 10 ps interval from the fraction of time that the heavy-atom distances of the hydrogen bonds were ≤ 3.0 Å and that the X-H---Y angle was within 60° of linearity.

Free energy calculations. The loss in docking free energy of a variant relative to the WT, $\Delta\Delta G_{\text{dock}}$, was calculated at 25 °C from the rate constants of docking and undocking, k_{dock} and k_{undock} , respectively, of the precursor ribozyme as accessible in single molecule FRET experiments (3-5):

$$\Delta\Delta G_{\text{dock}} = -RT \ln \left[\left(\frac{k_{\text{dock}}(\text{variant})}{k_{\text{undock}}(\text{variant})} \right) \times \left(\frac{k_{\text{undock}}(\text{WT})}{k_{\text{dock}}(\text{WT})} \right) \right],$$

where T is the temperature in Kelvin and R is the universal gas constant; the experimental errors were propagated forward to obtain the error bars in **Fig. 5**. The G+1A variant was never experimentally observed to dock, indicating that undocking is so fast that few docking events exceed our experimental time resolution of 100 ms(3). To estimate the underlying undocking rate constant, we assumed that 95% of all docking events go undetected and only 5% of them are equal to or exceed our experimental time resolution. As the undocking dwell times of all other hairpin ribozymes variants are well fit with one or more exponential curves, we back-calculated the undocking rate constant for a single-exponential decay of docking dwell times associated with 100% docked ribozymes at 0 ms and 5% left at 100 ms. This yielded a conservative lower estimate for $k_{\text{undock}}(\text{G+1A})$ of 23,000 s⁻¹. The error bars for $\Delta\Delta G_{\text{dock}}(\text{G+1A})$ were estimated by refitting the exponential decay with the fraction of ribozymes docked for ≥ 100 ms varying from 1% to 10% and by propagating this variance forward as error in $k_{\text{undock}}(\text{G+1A})$.

Interdomain cavity volumes. The interdomain cavity volumes for the individual simulations were calculated as van der Waals volumes using the software package VOIDOO (6). The cavity volume was obtained on structures averaged over the final 100 ps of each nanosecond of simulation; the value reported in the text is the average value over the course of a given simulation. Brief instances in a simulation where no cavity was found resulted in a zero volume that was included in both its mean volume and standard deviation.

Cleavage assays in sodium. Cleavage assays of the WT, dA38, dG11, and dC12 hairpin ribozyme variants in monovalent cations alone were conducted under single turnover conditions in 50 mM Tris-HCl, pH 7.5, over a three-hour time course at 25°C, essentially as described (5). Ribozyme (final concentrations: 100 nM strand RzA and 200 nM strand RzB) and radiolabeled substrate (<1 nM) were pre-annealed separately in standard buffer by heating to 70°C for 2 minutes and slow cooling over 5 min to room temperature. After pre-incubation for 15 min at 25°C, an equal volume of standard buffer containing labeled substrate was added to the ribozyme to initiate the reaction. 2 μL reaction aliquots were taken at appropriate time intervals and quenched with 13 μL stop solution (80% formamide, 0.025% xylene-cyanol, 0.025% bromophenol blue, and 50 mM EDTA). The 5' cleavage product was separated from uncleaved substrate by denaturing 20% polyacrylamide, 8 M urea, gel electrophoresis. $[\text{Na}^+]$ was incremented by 100 mM for each ribozyme variant from 0.1 to 1.4 M Na^+ . The extent of cleavage at three hours was quantified and normalized to the sum of the substrate and product bands using a PhosphorImager Storm 840 with ImageQuant software (Molecular Dynamics); it then was further normalized to the extent of cleavage of a given variant observed in 12 mM Mg^{2+} at three hours. The cleavage reactions in Mg^{2+} to which the sodium cleavage assays were normalized were conducted under single turnover conditions in standard buffer (50 mM Tris-HCl, pH 7.5, 12 mM Mg^{2+}) at 25°C. For **Fig. 6**, the sodium titrations of each ribozyme variant were fit with a simple binding equation as described (7) to illustrate the trend in level of activity observed.

Supporting Text

Additional structural details of variant simulations in the presence of Mg²⁺ suggest that expulsion of intracavity water may relate to diminished catalytic activity. Most simulated mutations were selected to disrupt major interdomain interactions (**Fig. 1a**). The 2'-deoxy-A38 (dA38) modification was chosen to disrupt a hydrogen bond with the pro-R_p non-bridging oxygen of the neighboring U39, so as to specifically affect the G+1 binding pocket of the docked structure without disrupting the interdomain base pair. Experimentally, the dA38 modification only modestly accelerates docking (2.3-fold) but drastically accelerates undocking 65-fold (5). Throughout the WT-Mg simulations we find that A38(2'OH) and U39(O2P) share a hydrogen bond, while A38(2'O) is also within 3.0 Å of G36(O2') for 26.4% of the time in the two simulations (**Figs. 2, 7**). In addition, portions of the G36 base remain within hydrogen bonding distance (3.5 Å) of A38(2'O) for up to 67% of the duration of simulations WT-Mg-1 and WT-Mg-2. In the variant simulation dA38-Mg the hydrogen replacing the deleted 2'-OH, A38(2'H2), also remains in proximity to U39(O2P) for 99.9% of the time; their mean distance increases by only 0.35Å to 3.05Å and the bond angle by 46° to 74°. By contrast, the proximity of A38(2'H2) to G36(O2') or any other atom of G36 is lost.

As described in the main text, in simulation dA38-Mg U42 loses contact with G11 and U12 in domain A despite the fact that these nucleotides are 13 Å and 15 Å away, respectively, from the point of mutation. The contacts of U42 with A22 and A23, which are in the same domain as U42 and slightly closer to the dA38 mutation, are also lost. The G+1:A38 stacking interaction, which was disrupted for three nanoseconds in simulation WT-Mg-1 so that water molecules entered the interdomain cavity (**Fig. 2e**), remains closed to water in simulation dA38-Mg (**Fig. 2c**); however, the A-1:G8 stacking interaction opens up early in the simulation, allowing water to enter. Despite the presence of these intracavity waters, the cavity volume decreases in simulation dA38-Mg by 70% (to 120±70 Å³) relative to the WT-Mg simulations (390±210 Å³; **Table 1**). The A-1 ribose retains its 2'-endo sugar pucker while the in-line attack angle (IAA) averages 129°.

The 2'-deoxy-G11 (dG11) modification was selected to disrupt two of the four hydrogen bonds in the ribose zipper, specifically those with A24, causing a modest 2-fold decrease in k_{dock} , but a more significant 12-fold increase in k_{undock} (5). In the dG11-Mg simulation, the A24(O2'):G11(2'H2) contact is inevitably lost. However, the bases slightly adjust by forming a hydrogen bond between A24(N1) and G11(N2) (**Fig. 2d**). The ribose zipper motif is thus not disrupted, despite the fact that it contains fewer hydrogen bonds than in the WT. Water molecules enter the core, but by different routes than in the WT simulations, for example passing G26. The local rearrangements around the ribose zipper cause the cavity volume to decrease by 55% (to 180±110 Å³; **Table 1**) relative to that of the WT. The A-1 ribose retains its 2'-endo sugar pucker while the IAA averages 132°.

The U42C mutation, not described in the main text in detail, was selected to disrupt the U42 binding pocket. It thus acts analogously to a 2'-deoxy-C12 (dC12) modification, which only slightly decelerates docking (by 43%), but significantly accelerates undocking 5.8-fold (5). Cross-correlation analysis of the U42-Mg simulation indicates that the interaction of nucleotide 42 with domain A is disrupted (**Figs. 9a, 9b**). Some rearrangements in the ribose zipper are also observed (**Fig. 9c**). A decrease in the overall extent of both correlations and anti-correlations relative to the WT is the result. However, the mutation's most noticeable effect is a reduction in the interdomain cavity volume by 82%, the greatest reduction by any of the mutant ribozymes (**Table 1**), which

accommodates only two water molecules next to G+1 and A-1 (**Fig. 16e**). The two base pairs of helix 4 adjacent to loop B show some fraying that is absent in the WT or any of the other variant simulations. The A-1 ribose maintains its 2'-endo sugar pucker.

The G+1A mutation, also not described in the main text in detail, was chosen to disrupt the interdomain G+1:C25 base pair and is, at an experimental time resolution of 100 ms, not observed to dock (3). This correlates with the fact that this is a structurally much disturbed variant in the G+1A-Mg simulation, where cross-correlation analysis indicates more anti-correlations present in this simulation than in any other simulation (**Fig. 8a**). All five major interdomain contacts are disrupted as the mutated nucleotide turns its Watson-Crick face away from C25 (and towards A10) within the first nanosecond of the simulation (**Fig. 8b**). The rotation of A+1 removes it from the G+1 binding pocket without separating the ribozyme's two domains spatially on the simulation timescale. Some of the eight disrupted RNA-RNA interdomain hydrogen bonds become effectively replaced by alternate hydrogen bonds, but four are lost entirely. The interdomain cavity shrinks to $150 \pm 70 \text{ \AA}^3$, and this is the only variant in which the cavity no longer borders A-1 or G+1 (**Fig. 8c**).

In summary, all simulated modifications and mutations decrease the volume of the interdomain cavity by $\geq 55\%$, in contrast to our observations for the WT (**Table 1**). In addition to the structural changes, this water expulsion may be related to the observed diminished catalytic rate constants (5).

Location and behavior of divalent cations. We replaced 6 Ca^{2+} ions found in the crystal structure with Mg^{2+} ions. The main distinctions between calcium and magnesium cations are the difference in size (1.0 \AA for a non-hydrated Ca^{2+} versus 0.7 \AA for a non-hydrated Mg^{2+} ; for hydrated cations, it is 4.1 \AA for Ca^{2+} and 4.3 \AA for Mg^{2+}), the difference in coordination number (8 for Ca^{2+} versus 6 for Mg^{2+}), and the higher polarizability of Ca^{2+} compared to Mg^{2+} . As the AMBER force field does not include polarizability in its parameter set, the latter distinction does not affect our simulations. As for coordination number, we did not retain the water molecules present in the solvation shells in the crystal structures. Instead, we added new solvent molecules and found that the Mg^{2+} cations consistently recruited and maintained the expected six water molecules in their solvation shells. Finally, the size difference of the hydrated cations is negligible. Furthermore, all simulations performed in the presence of divalent Mg^{2+} cations were also duplicated in the presence of Na^+ cations alone. Taken together, these observations suggest that, in the context of the approximations of an MD simulation (see below), replacing Ca^{2+} with Mg^{2+} ions appears legitimate.

Four of the six Mg^{2+} cations, those in the major groove by C+3, A22, A24, and A40, remain in their crystallographic locations throughout the six Mg^{2+} -containing simulations. The remaining two cations start out surrounded by bulk water since they were associated with parts of the crystallized RNA-U1A protein complex removed for the simulation. Throughout most simulations, these cations remain $\geq 10 \text{ \AA}$ distant from any interdomain interactions. Between 3.0 and 9.0 ns of simulation WT-Mg-1, a Mg^{2+} spends a total of 2.6 ns at a distance of 4-5 \AA from the G+1 phosphate, with one to two solvation shells of water molecules inserted between the ion and the ribozyme; at ~ 9 ns, the ion moves back towards bulk solvent and then, at 12 ns, over to the phosphate backbone of G6 and A7, where it remains for the rest of the simulation. This new position places it within 6 \AA of the Hoogsteen face of A-1.

A second fully solvated Mg^{2+} in simulation WT-MG-1 comes within 4.5 \AA of A10's phosphate backbone at 12 ns and remains there. In simulation dG11-Mg, a solvated Mg^{2+} approaches the G+1:A38 stacking interaction and stabilizes the two bases in a partially open

configuration at 3.5 ns. This cation stays within 4.0 to 4.5 Å of the phosphate oxygens of G+1 and A38. A water molecule outside of the cation's first solvation shell, but trapped between the solvated cation and the RNA, exchanges with an intracavity water molecule in the latter half of the simulation. Since this trapped water is on the same side of G+1 and A38 as bulk solvent, it was not counted or pictured among dG11-Mg's intracavity water molecules in the main text. None of the intracavity water molecules discussed in this work are within the first or second solvation shell of a divalent (or monovalent) cation, and no Mg²⁺ or Na⁺ cations enter the interdomain cavity during our simulations, except for the G+1A simulations where the cavity opens up to bulk solvent (**Table 1**).

Additional structural details on WT and variant simulations in Na⁺ support our conclusions from the Mg²⁺-containing simulations. The Na⁺-only simulations yield correlation matrices similar to those of their corresponding Mg²⁺-containing counterparts (**Figs. 10 to 15**). Cross-correlations and anti-correlations differ primarily in intensity, not in the nucleotides between which the correlations are observed. Attesting to the reproducibility of our simulation results and the generality of our conclusions, the cross-correlation matrix for each Na⁺ simulation was distinctly more similar to its Mg²⁺ counterpart than to any of the other matrices, with one exception. The correlations of dA38-Na (**Fig. 12a**), while still between the same nucleotides as those observed for dA38-Mg (**Fig. 1c**), show a decrease in anti-correlation intensity and increase in positive correlation intensity relative to simulation dA38-Mg sufficiently large for them to appear relatively similar to those of simulation dG11-Mg (**Fig. 13a**). Additionally, the correlation between U42 and domain A does not disappear as it does in simulation dA38-Mg. Nevertheless, the rotation of the U42 Watson-Crick face away from domain A observed in simulation dA38-Mg does occur in dA38-Na (as it does in two other sodium simulations, dG11-Na and G+1A-Na); yet U42(O4) retains the correlation to domain A by means of a water-mediated hydrogen bond to C-2 (**Fig. 16f**). This is the only interdomain water present in the simulation. Finally, the G11(N2):A24(N1) hydrogen bond in the ribose zipper that replaces G11(O2'):A24(O2') in dG11-Mg also appears in dA38-Na, although the original hydrogen bond is also retained (**Fig. 12c**).

Simulations WT-Na-1 and WT-Na-2 have similar results as the two WT-Mg simulations, both in terms of correlation matrices as well as the tertiary structure of the core. Small changes include decreases in cavity size and number of intracavity water molecules (**Table 1, Figs. 10, 11, 16a, b, c**). While the G+1:A9 water bridge is retained in both WT-Na-1 and WT-Na-2 and the A10:A38 water bridge is retained in WT-Na-2, there are no waters by the U42 pocket in either WT-Na-1 or WT-Na-2. In the case of WT-Na-1, the decreases are accompanied by a core-ward movement of U42 by 1 Å with no rotation of the base (**Figs. 9b, 9c**).

As noted above, the 180° rotation of U42 that occurs in both simulations dA38-Mg and dA38-Na is also observed in dG11-Na. The new G11(N2):A24(N1) hydrogen bond in the ribose zipper also appears in simulation dG11-Na; however, unlike the other simulations in which this hydrogen bond occurs, the hydrogen bond between the 2'-hydroxyls of G11 and A24 vanishes (**Fig. 13b**). The A10:A38 water bridge is retained, but the G+1:A9 water bridge which is highly occupied in the WT ribozyme, is lost (**Fig. 16g**).

Like its Mg²⁺ containing counterpart G+1A-Mg, the cross-correlation matrix of G+1A-Na displays several regions of anti-correlated behavior (**Fig. 14a**). The majority of the interdomain hydrogen bonds are lost early in both simulations; however, in G+1A-Na, the ribose zipper motif is also lost, resulting in the domain A portion of the zipper moving 10-12 Å away from the corresponding part of domain B after 10 ns. Two interdomain hydrogen bonds that remain in simulation G+1A-Na are A23(N6):U42(O4) and G+1A(N7):C25(N4). Rotation of the U42 base

occurs in G+1A-Na, though the rotation is nearer 90° than the 180° observed in simulations dA38-Mg, dA38-Na, and dG11-Na (**Fig. 14c**). No long-term intracavity water molecules are observed; in fact, the cavity becomes exposed to bulk solvent during the simulation allowing for the entry of a single Na⁺ ion (**Table 1**).

In simulation U42C-Na, some rearrangements in the ribose zipper are observed (**Fig. 15c**). A decrease in the overall extent of correlations and anti-correlations relative to the WT is observed, although more correlations remain in simulation U42C-Na than in U42C-Mg. While the interactions of a C42 with domain A are not lost in the Na⁺ simulation (**Fig. 15a**) as they are in the Mg²⁺-containing counterpart U42C-Mg (**Fig. 9a**), the direct hydrogen bond that is present between U42(O4) and G11(N2) in the WT simulation is lost as it is in U42C-Mg; U42C(N4) remains correlated with domain A only through a hydrogen bond to A24 and its participation in the ribose zipper (**Fig. 15c**). In simulation U42C-Mg the size of the interdomain cavity is reduced to 30% of that of WT-Mg; in U42C-Na, it is reduced to only 13% ($50\pm 60 \text{ \AA}^3$; **Table 1**). Only one water molecule, participating in a G+1:A10 water bridge, is observed in the interdomain cavity (**Fig. 16i**).

Systematic changes across all Na⁺-only simulations may pertain to decreased catalytic activity in low Na⁺. The effective cation concentrations are 260 mM Na⁺ in the Na⁺-only simulations and 30 mM Mg²⁺ and 200 mM Na⁺ in the Mg²⁺-containing simulations. Experimentally, the ribozymes are less catalytically active in 260 mM Na⁺ than they are in 30 mM Mg²⁺ (**Fig. 6**). Thus, any systematic changes across the six sodium simulations relative to the six Mg²⁺ simulations may well indicate differences that adversely impact activity. We observe three such systematic changes: (i) a decrease in the size of the interdomain cavity; (ii) a corresponding decrease in the number of intracavity waters; and (iii) the loss of the G+1:A9 water bridge in the modified and mutant ribozymes simulated in Na⁺.

More specifically, the volume of the interdomain cavity decreases by 40% from $390\pm 210 \text{ \AA}^3$ in the WT-Mg simulations to $225\pm 100 \text{ \AA}^3$ in the two WT-Na simulations (**Table 1**). There is a corresponding drop in the number of intracavity water molecules (**Figs. 16b, 16c**). The remaining water molecules are in close proximity to G+1, A9, and A10 as well as the 2'-hydroxyl of A-1, which faces into the interdomain cavity in both WT-Na simulations. The interdomain cavities in the sodium simulations of the variant ribozymes also typically decrease in size relative to their Mg²⁺-containing counterparts, even vanishing completely for portions of simulations dA38-Na and U42C-Na. That is, the cavity volume in simulation dA38-Na ($50\pm 90 \text{ \AA}^3$) decreases by 60% relative to that of dA38-Mg; the cavity volumes of simulations U42C-Na ($50\pm 60 \text{ \AA}^3$) and dG11-Na ($160\pm 50 \text{ \AA}^3$) decrease by 30% and 10% relative to U42C-Mg and dG11-Mg, respectively. All interdomain cavity volumes in the modified or mutant ribozymes in Na⁺ are $\leq 71\%$ of the size of the cavity in WT-Na and $\leq 40\%$ of the cavity volume of WT-Mg. In dA38-Na and U42C-Na, the number of intracavity water molecules observed simultaneously decrease from two to one or none, while the waters decrease from three in dG11-Mg to two in dG11-Na (**Fig. 10**).

Intracavity water locations in our MD simulations compare well with those in a recent high-resolution crystal structure. Intracavity hydrogen-bonding sites for water molecules that are filled during the WT-Mg simulations are less frequently occupied during other simulations. A single hydration site connects A26(N3) and the water molecules in the G+1-A9 bridge; two or three water molecules are shared between U42, A40, and G11. The A26-bonded hydration site is observed in simulations WT-Mg-1, WT-Mg-2, WT-Na, dG11-Mg and G+1A-Mg, while the U42-associated water molecules appear only in the WT-Mg simulations (**Fig. 16**). Water

molecules entering the ribozyme within the first nanosecond of simulation are possibly part of the equilibration process. However, water molecules both enter and exit the interdomain cavity after four nanoseconds of simulation WT-Mg-1 (**Fig. 17**), suggesting that they begin to equilibrate. The number of water molecules resident in the WT simulations appears to stabilize at five or six waters as the simulation progresses. Indeed, the intracavity waters are in number and position similar to the five found in the recent, higher-resolution crystal structure of the junctionless ribozyme (2), despite the fact that we started our simulations with an empty interdomain cavity. For example, water 86 of the crystal structure is located in proximity to the G+1:A9 water bridge in our WT simulations, while the crystallographic waters 54 and 55 correspond to the A10:A38 water bridge in our MD simulations (**Fig. 17**). The crystallographic water 52 is located between these two primary water bridges of the simulations. Finally, the crystallographic water 45 occupies a position corresponding to the averaged position of the three U42 waters in our WT-Mg simulations (**Fig. 17**) (2).

Such a significant consistency between simulation and experiment is even more compelling in light of the fact that our simulations are performed at room temperature in solution, while x-ray diffraction is performed on a frozen, essentially solid-state crystal.

Ribose pucker analysis. As noted in the main text, during simulations of the WT hairpin ribozyme, the ribose of the A-1 nucleotide changes from the C2'-endo conformation to the thermodynamically more stable C2'-exo conformation, common in double-stranded RNA, and the sugar pucker remains in that conformation thereafter. To test if this conformational change results from a bias in the force field towards the C2'-exo conformation, we determined the pseudorotational sugar pucker of all 56 nucleotides for all four WT simulations and for the four simulations of modified ribozymes in the presence of both Mg²⁺ and Na⁺. 76% of all riboses start and end simulations in the C2'-exo conformation, while 8% remain in the C2'-endo conformation throughout (**Table 2**). 15% of riboses switch conformation at least once during a given simulation; switches both towards and away from the C2'-exo conformation are observed (**Tables 3-5**). While these observations do not exclude the possibility of a minor force field bias, they indicate that any such bias is not sufficiently strong to either generally convert C2'-endo riboses into the more stable C2'-exo riboses or to keep them in the C2'-exo conformation over extended periods of time. Experimentally, the kinetic barrier between the two sugar pucker conformations is small enough (~4 kcal/mol)(8) to allow for interconversion over short timescales, consistent with the behavior in our MD simulations.

While the sugar puckers of other riboses thus readily interconvert between the 2'-endo and 2'-exo conformations, the A-1 ribose changes to 2' exo and remains in that conformation in all of our four WT simulations; only in the structurally highly perturbed G+1A-Mg simulation does the A-1 ribose freely interconvert (**Table 2**). This suggests that the switch of the catalytic hydroxyl of A-1 in the WT simulations from 2'-endo to 2'-exo is significant and indicative of a realistic structural conversion. It may be triggered by the additional hydrogen bonding capacity of the 2'-OH in our MD simulations relative to the 2'-O-methyl modification of the starting crystal structure. Another relevant sugar pucker change is that of A38. This sugar pucker differs in the junctionless and four-way junction crystal structure of the hairpin ribozyme. In the four-way junction crystal structure that served as starting structure for our MD simulations, the A38 ribose is in the 2'-endo conformation, but in the crystal structure of the junctionless ribozyme A38 is in a 2'-exo conformation (1, 2). Notably, in all eight simulations in which we analyzed the sugar

puckers, the A38 ribose makes a switch to an O4'-endo conformation, intermediate between the two sugar puckers observed crystallographically for A38 (Table 5).

Control simulation with a sodium cation replacing an intracavity water molecule. A control simulation in which we deliberately placed a Na⁺ cation within the cavity of the WT hairpin ribozyme found that it remained within the cavity throughout 31 ns of simulation (data not shown) so that we cannot rule out that a partly desolvated Na⁺ cation may occasionally get caught in the cavity during docking. This control simulation was derived from the WT-Na-2 simulation, where one of the three intracavity water molecules (the one seen hydrogen bonded to A-1 and A38 in Fig. 16c) was replaced by a Na⁺ cation. The entire complex was reequilibrated and then MD simulated for 31 nanoseconds.

The intracavity sodium cation remained in the cavity; however, the general trend for it was to move away from the 2'-OH of A-1 and towards the G+1:A38 stacking interaction, which represents the dominant entry and exit gate for water molecules. The distance from the cation to the A-1 hydroxyl grew from 2.3 Å at the start to 3.5 Å at the end of the control simulation. No additional water molecules entered into the internal cavity during the 31 ns of simulation and the two water molecules already in the internal cavity remain within 0.5 Å of their initial positions. One of these two intercavity water molecules participates in the A10:A38 water bridge that was present in the majority of the simulations of the WT hairpin ribozyme and its catalytically active variants; the position is equivalent to that of water I in Fig. 17. The other remaining intracavity water molecule participates in the G+1:A9 water bridge, which is also a commonly filled position (water D in Fig. 17). The two intracavity water molecules of the control simulation are within 2.5 to 3 Å of the Na⁺ cation, which puts them within its first solvation shell. The catalytic core has an RMSD of 0.6 Å with respect to its starting structure from WT-Na-2. The major hydrogen bonding and stacking interactions remain intact during the control simulation. As occurs in WT-Na-2 but not WT-Na-1, there are no hydrogen bonds between U42 and both U12 and A22. However, the U42 binding pocket is generally the tertiary interaction motif with the least stable hydrogen bonds in our MD simulations. Taken together, our observations on the control simulation suggest that the overall structure is not significantly perturbed by the occasional capture of a largely desolvated Na⁺ ion in the interdomain cavity; yet partially desolvating a Na⁺ will be associated with a significant energetic penalty, making such capture a relatively unlikely event. Therefore, the long-residency intracavity water molecules are exposed to a largely unshielded negative surface potential in the catalytic core, supporting our hypothesis that their pK_a's are likely perturbed and they are poised for protonation.

General considerations for molecular dynamics simulations. When evaluating the present MD simulation results, it is important to keep in mind that their outcome may be affected by approximations and limitations. First, approximations originate from the use of simple pair-additive empirical potential functions. However, the Cornell et al. force field is thought to provide a balanced description of base stacking and H-bonding, superior to other force fields (9). Additional care needs to be taken regarding the backbone description. The backbone is described by a set of simple torsional functions and its behavior may be further affected by the use of conformation-independent atom-centered electrostatic-potential derived point charges. While such a charge model is entirely sufficient for base stacking and H-bonding of rigid nucleobases, its application to a flexible and anionic backbone chain is less realistic, as constant charges cannot fully describe the changes in electrostatic potential in response to changes in geometry. In fact, accumulation of long-lived backbone flips was recently reported in extended B-DNA simulations

(10). We thus very carefully monitored the behavior of the backbone dihedral angles and concluded that no unusual or excessive backbone flips occurred in our present or preceding simulations of various RNA molecules (11-17). This suggests that RNA simulations, at least on the current state-of-the-art timescale, are structurally meaningful.

Second, a potential limitation is the current nanosecond-scale of simulations that prevents the crossing of more substantial free energy barriers. This suggests that our simulations are likely not sufficiently long to achieve a representative sampling of large-scale motions such as, for example, domain undocking. However, the near-perfect linear correlation (correlation coefficient $r = 0.98$) between the number of lost hydrogen bonds in our simulations and the loss in docking free energy relative to the WT, determined from single molecule FRET experiments (**Fig. 5**), implies that our 10-ns MD simulations starting from the docked crystal structure indeed provide plausible models for the structures probed in docking experiments.

Third, a problem is presented by Mg^{2+} cations that are poorly represented by simple force fields, since major polarization and charge transfer effects are neglected. As shown recently (13), improperly placed Mg^{2+} can cause substantial perturbations of a simulated RNA structure, which are not repaired in the course of the simulation. For this reason, the present analysis was based on both Mg^{2+}/Na^+ and Na^+ -only containing simulations, which gave consistent results and in conjunction support our conclusions.

It is important to realize that our MD simulations are one of only very few biophysical tools that can probe the location and dynamic behavior of water molecules as they pertain to structure and function of a biopolymer. Our observations suggest that they indeed represent a powerful tool to this end if used correctly and cautiously. MD simulations thus provide guidance for future experimental studies and complement the static pictures obtained by x-ray crystallography.

Supporting References:

1. Rupert, P. B. & Ferre-D'Amare, A. R. (2001) *Nature* **410**, 780-786.
2. Salter, J., Krucinska, J., Alam, S., Grum-Tokars, V. & Wedekind, J. E. (2006) *Biochemistry* **45**, 686-700.
3. Zhuang, X., Kim, H., Pereira, M. J., Babcock, H. P., Walter, N. G. & Chu, S. (2002) *Science* **296**, 1473-1476.
4. Bokinsky, G., Rueda, D., Misra, V. K., Rhodes, M. M., Gordus, A., Babcock, H. P., Walter, N. G. & Zhuang, X. (2003) *Proc. Natl. Acad. Sci. USA* **100**, 9302-9307.
5. Rueda, D., Bokinsky, G., Rhodes, M. M., Rust, M. J., Zhuang, X. & Walter, N. G. (2004) *Proc. Natl. Acad. Sci. USA* **101**, 10066-10071.
6. Kleywegt, G. J. & Jones, T. A. (1994) *Acta Cryst. D* **50**, 178-185.
7. Tinsley, R. A., Harris, D. A. & Walter, N. G. (2004) *Biochemistry* **43**, 8935-8945.
8. Olson, W. K. (1982) *J. Am. Chem. Soc.* **104**, 278-286.
9. Cornell, W. D., Cieplak, P., Bayly, C. I., Gould, I. R., Merz, K. M., Ferguson, D. M., Spellmeyer, D. C., Fox, T., Caldwell, J. W. & Kollman, P. A. (1995) *J. Am. Chem. Soc.* **117**, 5179-5197.
10. Varnai, P. & Zakrzewska, K. (2004) *Nucleic Acids Res.* **32**, 4269-4280.
11. Reblova, K., Spackova, N., Sponer, J. E., Koca, J. & Sponer, J. (2003) *Nucleic Acids Res.* **31**, 6942-6952.

12. Reblova, K., Spackova, N., Stefl, R., Csaszar, K., Koca, J., Leontis, N. B. & Sponer, J. (2003) *Biophys. J.* **84**, 3564-3582.
13. Reblova, K., Spackova, N., Koca, J., Leontis, N. B. & Sponer, J. (2004) *Biophys. J.* **87**, 3397-3412.
14. Krasovska, M. V., Sefcikova, J., Spackova, N., Sponer, J. & Walter, N. G. (2005) *J. Mol. Biol.* **351**, 731-748.
15. Razga, F., Koca, J., Sponer, J. & Leontis, N. B. (2005) *Biophys. J.* **88**, 3466-3485.
16. Spackova, N. & Sponer, J. (2006) *Nucleic Acids Res.* **34**, 697-708.
17. Krasovska, M. V., Sefcikova, J., Reblova, K., Schneider, B., Walter, N. G. & Sponer, J. (2006) *Biophys. J.* **91**, 626-638.

Supporting Table 1. Overview of the MD simulations performed in this study

Simulation	Duration (ns)	Ions present	Average cavity volume \pm s.d. (\AA^3)	# of intracavity waters	# of intracavity Na^+ ions
WT-Mg-1	30	6 Mg^{2+} , 41 Na^+	340 \pm 180	7 (at 10 ns) 5 (at 20 ns) 5 (at 30 ns)	0
WT-Mg-2	10	6 Mg^{2+} , 41 Na^+	450 \pm 230	5 (at 10 ns)	0
WT-Na-1	10	53 Na^+	210 \pm 110	2 (at 10 ns)	0
WT-Na-2	10	53 Na^+	240 \pm 100	3 (at 10 ns)	0
dA38-Mg	14.75	6 Mg^{2+} , 41 Na^+	120 \pm 70	2 (at 10 ns) 2 (at 14.75 ns)	0
dA38-Na	10	53 Na^+	50 \pm 90	1 (at 10 ns)	0
dG11-Mg	10	6 Mg^{2+} , 41 Na^+	180 \pm 110	3 (at 10 ns)	0
dG11-Na	10	53 Na^+	160 \pm 50	2 (at 10 ns)	0
G+1A-Mg	13.8	6 Mg^{2+} , 41 Na^+	150 \pm 70	2 (at 10 ns) 3 (at 13.8 ns)	1 ^a
G+1A-Na	10	53 Na^+	N/A	0	1 ^a
U42C-Mg	10	6 Mg^{2+} , 41 Na^+	120 \pm 70	2 (at 10 ns)	0
U42C-Na	10	53 Na^+	50 \pm 60	1 (at 10 ns)	0

^aIn these simulations the interdomain cavity opened up to the bulk solution.

Supporting Table 2. Percentage of riboses in the hairpin ribozyme that have the specified sugar puckers during the listed simulations.

Simulation	WT-Mg-1	WT-Mg-2	dA38-Mg	dG11-Mg	G+1A-Mg	U42C-Mg	WT-Na-1	WT-Na-2	Overall
Riboses always 2'-exo	73%	75%	77%	79%	77%	77%	75%	75%	76%
Riboses always 2'-endo	9%	7%	5%	7%	5%	7%	11%	12.5%	8%
Riboses that switch conformation	18%	18%	16%	12.5%	18%	14%	12.5%	11%	15%

Supporting Table 3. Pseudorotational sugar puckers of nucleotides in the substrate strand that are not exclusively in the 2'-exo conformation during the eight listed simulations.

Nt	WT-Mg-1	WT-Mg-2	dA38-Mg	dG11-Mg	G+1A-Mg	U42C-Mg	WT-Na-1	WT-Na-2
U-5	2'-exo to 2'-endo	Switches between 2'-endo and 2'-exo	2'-exo	2'-exo	2'-exo to 2'-endo	Switches between 2'-exo and 2'-endo	2'-exo to 2'-endo	2'-exo
A-1	2'-endo to 2'-exo	2'-endo to 2'-exo	2'-endo	2'-endo	Switches between 2'-endo and 2'-exo	2'-endo	2'-endo to 2'-exo	2'-endo to 2'-exo
G+1	2'-endo to O4'-endo	2'-exo to C1'-exo	2'-endo	2'-endo	2'-endo to 2'-exo	2'-endo	2'-endo	2'-endo
C+4	2'-exo	Switches between 2'-endo and 2'-exo	2'-exo	2'-exo	2'-exo	2'-exo	2'-exo	Switches between 2'-endo and 2'-exo
U+5	2'-exo to 2'-endo to 2'-exo	2'-exo	2'-exo	2'-exo	2'-exo	2'-exo	2'-exo	2'-exo to 2'-endo to 2'-exo
C+6	2'-exo switches rapidly with 2'-endo	2'-exo switches rapidly with 2'-endo	2'-exo switches rapidly with 2'-endo	2'-exo switches rapidly with 2'-endo	2'-exo switches rapidly with 2'-endo	2'-exo switches rapidly with 2'-endo	2'-exo switches rapidly with 2'-endo	2'-exo switches rapidly with 2'-endo

Supporting Table 4. Pseudorotational sugar puckers of nucleotides in ribozyme strand A that are not exclusively in the 2'-exo conformation during the eight listed simulations.

Nt	WT-Mg-1	WT-Mg-2	dA38-Mg	dG11-Mg	G+1A-Mg	U42C-Mg	WT-Na-1	WT-Na-2
A9	2'-exo to C4'-exo	2'-exo	2'-exo	2'-exo	2'-exo	2'-exo	2'-exo	2'-exo
A14	2'-endo	2'-endo to 2'-exo to 2'-endo	2'-endo to 2'-exo to 2'-endo	2'-endo to 2'-exo to 2'-endo	2'-endo	2'-exo to 2'-endo	2'-endo	2'-endo
C27	2'-exo	2'-exo	2'-exo to 2'-endo	2'-exo	2'-exo	2'-exo	2'-exo to 2'-endo to 2'-exo	2'-exo
A28	2'-exo	2'-exo	2'-exo to O4'-exo	2'-exo	2'-exo	2'-exo	2'-exo	2'-exo
C29	2'-exo	2'-exo	2'-exo to 2'-endo	2'-exo	2'-exo	2'-exo to 2'-endo	2'-exo	2'-exo
C30	Switches between 2'-endo and 2'-exo	Switches between 2'-endo and 2'-exo	Switches between 2'-endo and 2'-exo	Switches between 2'-endo and 2'-exo	Switches between 2'-endo and 2'-exo	Switches between 2'-endo and 2'-exo	Switches between 2'-endo and 2'-exo	Switches between 2'-endo and 2'-exo

Supporting Table 5. Pseudorotational sugar puckers of nucleotides in ribozyme strand B that are not exclusively in the 2'-exo conformation during the eight listed simulations.

Nt	WT-Mg-1	WT-Mg-2	dA38-Mg	dG11-Mg	G+1A-Mg	U42C-Mg	WT-Na-1	WT-Na-2
U34	2'-exo to 2'-endo to 2'-exo	2'-exo	2'-exo	2'-exo	2'-exo	2'-exo	2'-exo	2'-exo
G35	2'-exo	2'-exo	2'-exo	2'-exo	2'-exo to 2'-endo	Switches between 2'-endo and 2'-exo	Switches between 2'-exo and 2'-endo	2'-exo
U36	2'-exo	Switches between 2'-endo and 2'-exo	2'-exo	2'-endo to 2'-exo	2'-endo to 2'-exo	2'-exo	2'-endo	2'-endo
U37	2'-endo	2'-endo	Switches between 2'-endo and 2'-exo	2'-endo to C4'-exo to 2'-endo	2'-exo to 2'-endo	Switches between 2'-endo and 2'-exo	2'-endo	2'-endo
A38	2'-endo to O4'-endo	2'-endo to O4'-endo	O4'-endo	O4'-endo	C1'-exo to O4'-endo to C1'-exo	O4'-endo	O4'-endo	O4'-endo
U39	2'-endo	2'-endo	2'-endo	2'-endo	2'-endo	2'-endo	2'-endo	2'-endo
U41	2'-endo	2'-endo	2'-exo	2'-exo to 2'-endo	2'-exo	2'-exo	2'-exo	2'-exo
U42	2'-endo	2'-endo	2'-endo to C4'-exo to 2'-endo	2'-endo	2'-endo	2'-endo	2'-endo	2'-endo
U49	Switches between 2'-endo and 2'-exo	Switches between 2'-endo and 2'-exo	Switches between 2'-endo and 2'-exo	Switches between 2'-endo and 2'-exo	Switches between 2'-endo and 2'-exo	Switches between 2'-endo and 2'-exo	Switches between 2'-endo and 2'-exo	Switches between 2'-endo and 2'-exo

Supplementary Figure Legend:

Fig. 4. Molecular dynamics (MD) simulations of the hairpin ribozyme. **(a)** Secondary and tertiary structure of the simulated docked WT hairpin ribozyme (orange, substrate) (1); gray segments were present in our smFRET experiments, but omitted in MD. Solid horizontal lines represent Watson-Crick base pairs. Specific hydrogen bond interactions are annotated with circles (Watson-Crick), squares (Hoogsteen), and triangles (sugar edge), either filled (cis-interaction) or open (trans-interaction). Dashed lines represent single hydrogen bonds; dashed bent arrows represent backbone turns; the orange arrow marks the cleavage site. **(b)** RMSDs over 10 ns of MD simulation relative to the crystal structure and averaged by nucleotide for each of our Mg^{2+} -containing simulations (top two panels); compared with B (“temperature”) factors by nucleotide from the two available pre-catalytic crystal structure (bottom panel)(1, 2). Gray arrows indicate the 5'→3' direction of the 5' and 3' segments of each structural element. **(c)** Cross-correlation analyses by nucleotide of the first 10 nanoseconds of three representative MD simulations (WT-Mg-1, dA38-Mg, and dG11-Mg). The scale and specific cross-correlations for the interdomain interactions of these simulations and of WT-Mg-2 are shown as insets.

Fig. 5. Plot of the docking free energy loss relative to the WT ($\Delta\Delta G_{\text{dock}}$), derived from our single molecule FRET experiments (4, 5) versus the net lost number of interdomain tertiary hydrogen bonds after each 10 ns of MD simulation. Linear regression fits the data with a slope of 2.43 kcal/(mol lost hydrogen bond).

Fig. 6. Sodium titration of cleavage activity. The extent of cleavage by the WT and three modified hairpin ribozymes in varying Na^+ concentrations is normalized with respect to the typical extent of cleavage (at 3 hrs) by the variant of the ribozyme in 12 mM Mg^{2+} . The fits are with a simple binding equation (7) to qualitatively illustrate the trends.

Fig. 7. Analysis of simulation WT-Mg-2. **(a)** Cross-correlation analysis by nucleotide of MD simulation WT-Mg-2. The scale is shown as inset. **(b)** Specific distance density plots as indicated over the first 10 ns of the simulation; the color scale is shown as inset. At 9.0-9.1 ns (cyan line), a snapshot **(c)** of key nucleotides was averaged over each 100 ps where taken and overlaid (in color) over the starting, equilibrated WT crystal structure (silver); crystal structure hydrogen bonds that are maintained throughout the simulation are shown in green, those broken during the simulation are in red.

Fig. 8. Analysis of simulation G+1A-Mg. **(a)** Cross-correlation analysis by nucleotide of MD simulation G+1A-Mg. The scale is shown as inset. **(b)** Specific distance density plots as indicated over the first 10 ns of the simulation; the color scale is shown as inset. At 9.9-10 ns (cyan line), a snapshot **(c)** of key nucleotides was averaged over each 100 ps where taken and overlaid (in color) over the starting, equilibrated WT crystal structure (silver); crystal structure hydrogen bonds that are maintained throughout the simulation are shown in green, those broken during the simulation are in red. The yellow sphere is the single Na^+ cation noted in Table 1.

Fig. 9. Analysis of simulation U42C-Mg. (a) Cross-correlation analysis by nucleotide of MD simulation U42C-Mg. The scale is shown as inset. (b) Specific distance density plots as indicated over the first 10 ns of the simulation; the color scale is shown as inset. At 9.9-10 ns (cyan line), a snapshot (c) of key nucleotides was averaged over each 100 ps where taken and overlaid (in color) over the starting, equilibrated WT crystal structure (silver); crystal structure hydrogen bonds that are maintained throughout the simulation are shown in green, those broken during the simulation are in red.

Fig. 10. Analysis of simulation WT-Na-1. (a) Cross-correlation analysis by nucleotide of MD simulation WT-Na-1. The scale is shown as inset. (b) Specific distance density plots as indicated over the first 10 ns of the simulation; the color scale is shown as inset. At 9.0-9.1 ns (cyan line), a snapshot (c) of key nucleotides was averaged over each 100 ps where taken and overlaid (in color) over the starting, equilibrated WT crystal structure (silver); crystal structure hydrogen bonds that are maintained throughout the simulation are shown in green, those broken during the simulation are in red.

Fig. 11. Analysis of simulation WT-Na-2. (a) Cross-correlation analysis by nucleotide of MD simulation WT-Na-2. The scale is shown as inset. (b) Specific distance density plots as indicated over the first 10 ns of the simulation; the color scale is shown as inset. At 9.9-10 ns (cyan line), a snapshot (c) of key nucleotides was averaged over each 100 ps where taken and overlaid (in color) over the starting, equilibrated WT crystal structure (silver); crystal structure hydrogen bonds that are maintained throughout the simulation are shown in green, those broken during the simulation are in red.

Fig. 12. Analysis of simulation dA38-Na. (a) Cross-correlation analysis by nucleotide of MD simulation dA38-Na. The scale is shown as inset. (b) Specific distance density plots as indicated over the first 10 ns of the simulation; the color scale is shown as inset. At 9.9-10 ns (cyan line), a snapshot (c) of key nucleotides was averaged over each 100 ps where taken and overlaid (in color) over the starting, equilibrated WT crystal structure (silver); crystal structure hydrogen bonds that are maintained throughout the simulation are shown in green, those broken during the simulation are in red.

Fig. 13. Analysis of simulation dG11-Na. (a) Cross-correlation analysis by nucleotide of MD simulation dG11-Na. The scale is shown as inset. (b) Specific distance density plots as indicated over the first 10 ns of the simulation; the color scale is shown as inset. At 9.9-10 ns (cyan line), a snapshot (c) of key nucleotides was averaged over each 100 ps where taken and overlaid (in color) over the starting, equilibrated WT crystal structure (silver); crystal structure hydrogen bonds that are maintained throughout the simulation are shown in green, those broken during the simulation are in red.

Fig. 14. Analysis of simulation G+1A-Na. (a) Cross-correlation analysis by nucleotide of MD simulation G+1A-Na. The scale is shown as inset. (b) Specific distance density plots as indicated over the first 10 ns of the simulation; the color scale is shown as inset. At 9.9-10 ns (cyan line), a snapshot (c) of key nucleotides was averaged over each 100 ps where taken and overlaid (in color) over the starting, equilibrated WT crystal structure (silver); crystal structure hydrogen bonds that are maintained throughout the simulation

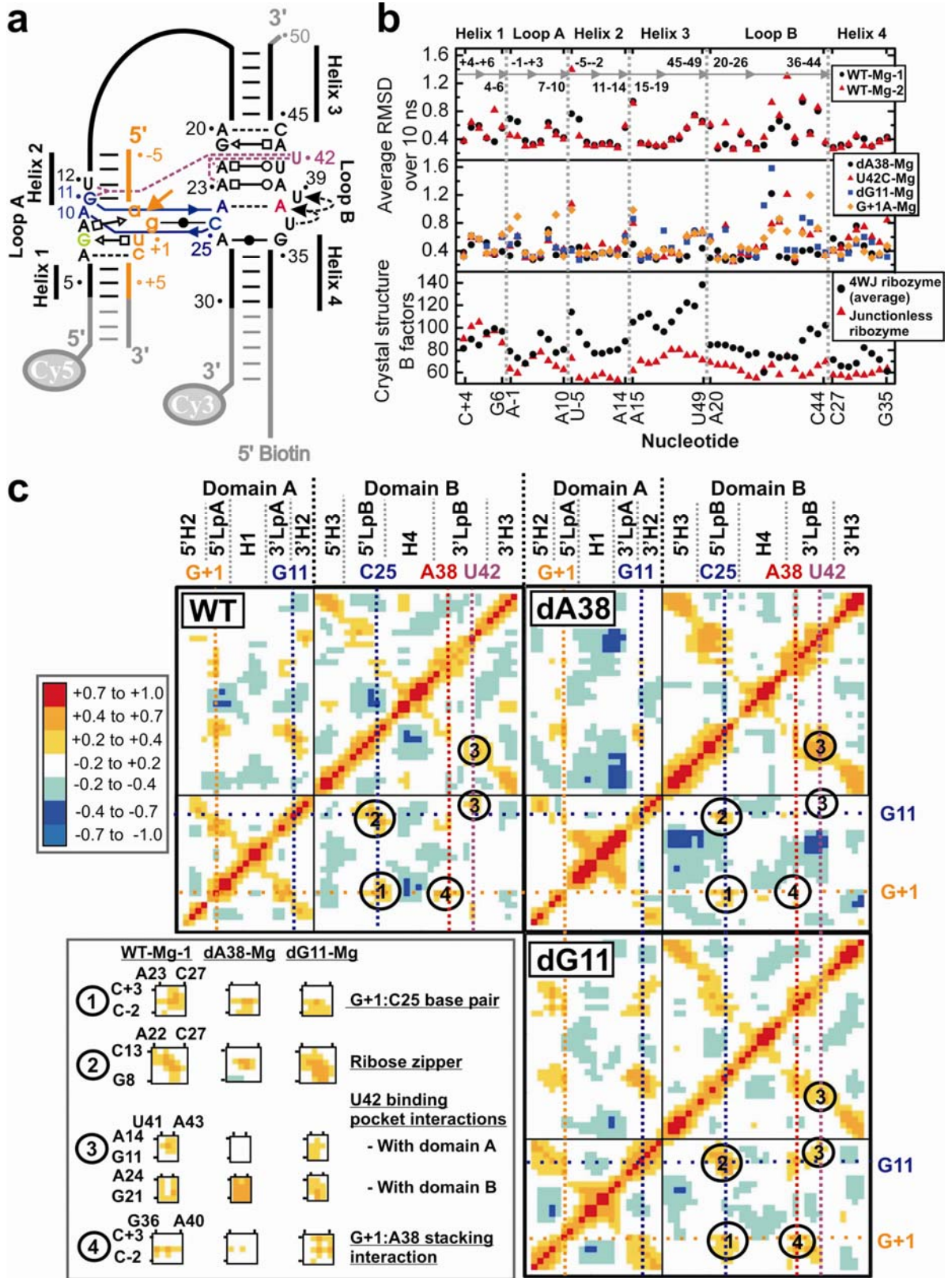
are shown in green, those broken during the simulation are in red. The yellow sphere is the single Na⁺ cation noted in Table 1.

Fig. 15. Analysis of simulation U42C-Na. **(a)** Cross-correlation analysis by nucleotide of MD simulation U42C-Na. The scale is shown as inset. **(b)** Specific distance density plots as indicated over the first 10 ns of the simulation; the color scale is shown as inset. At 9.9-10 ns (cyan line), a snapshot **(c)** of key nucleotides was averaged over each 100 ps where taken and overlaid (in color) over the starting, equilibrated WT crystal structure (silver); crystal structure hydrogen bonds that are maintained throughout the simulation are shown in green, those broken during the simulation are in red.

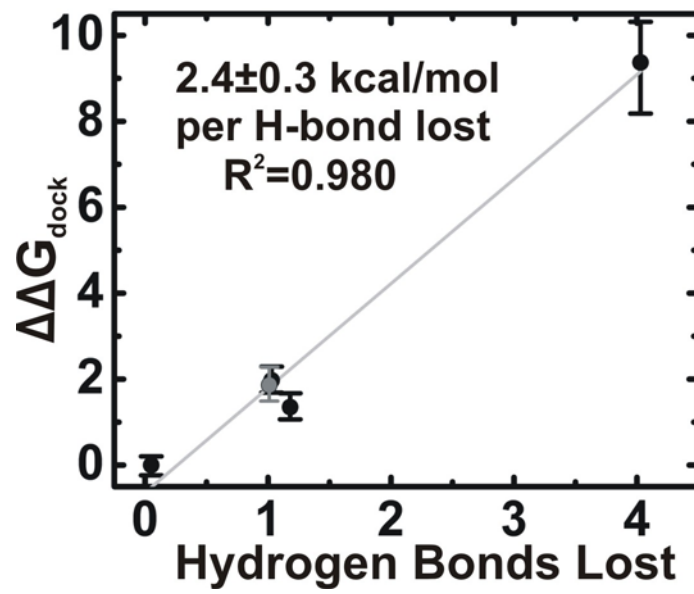
Fig. 16. Snapshots, averaged over the specified 100 ps of the remaining MD simulations, with the hydrogen bonding network of intracavity water molecules indicated in green. **(a)** WT-Mg-2 (averaged from 9.0 to 9.1 ns); **(b)** WT-Na-1 (averaged from 9.0 to 9.1 ns), **(c)** WT-Na-2 (9.9 to 10.0 ns), **(d)** G+1A-Mg (9.9 to 10 ns), **(e)** U42C-Mg (9.9 to 10.0 ns), **(f)** dA38-Na (9.9 to 10 ns), **(g)** dG11-Na (9.9 to 10 ns), **(h)** G+1A-Na (9.9 to 10 ns), and **(i)** U42C-Na (9.9 to 10 ns). The yellow spheres in **(d)** and **(h)** are Na⁺ cations.

Fig. 17. Snapshot of selected bases of the hairpin ribozyme and seven of its ten tracked water molecules averaged over 100 ps (7.9-8 ns) in WT-Mg-1 (thick bases and red-and-white waters) overlaying the crystal structure of the junctionless ribozyme (2) (thin grey bases) and its waters (yellow dots). The times of entry and exit of individual water molecules into and from the catalytic core are given in the inset.

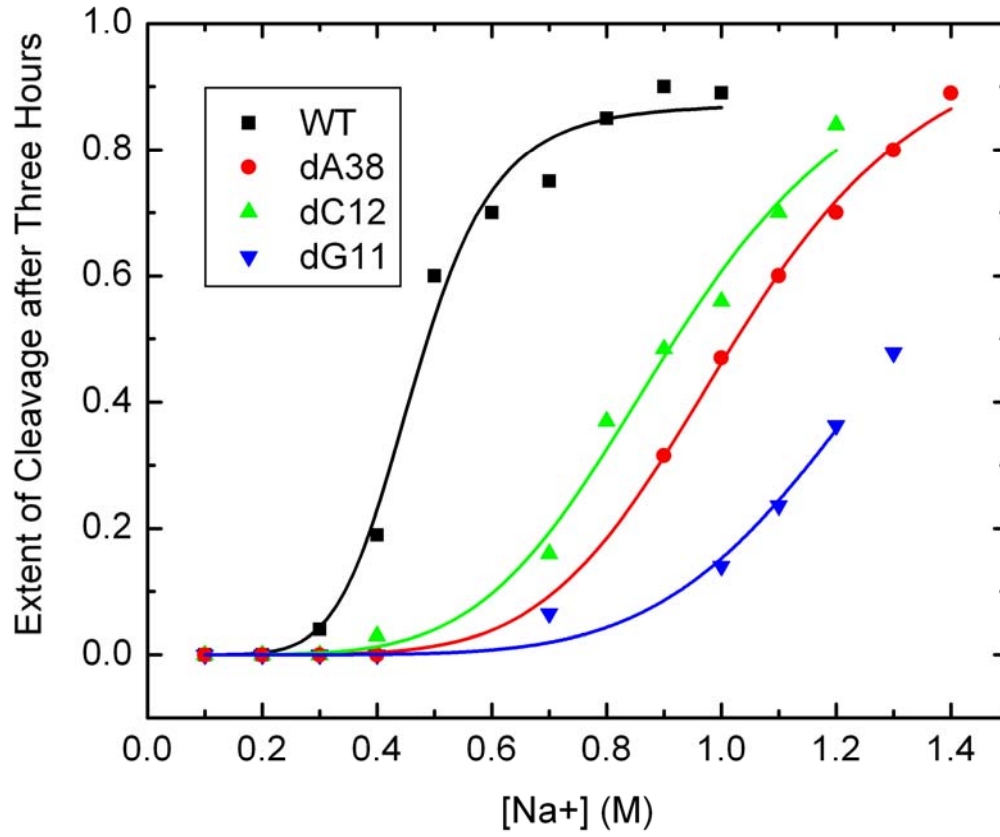
Rhodes et al., Figure 4



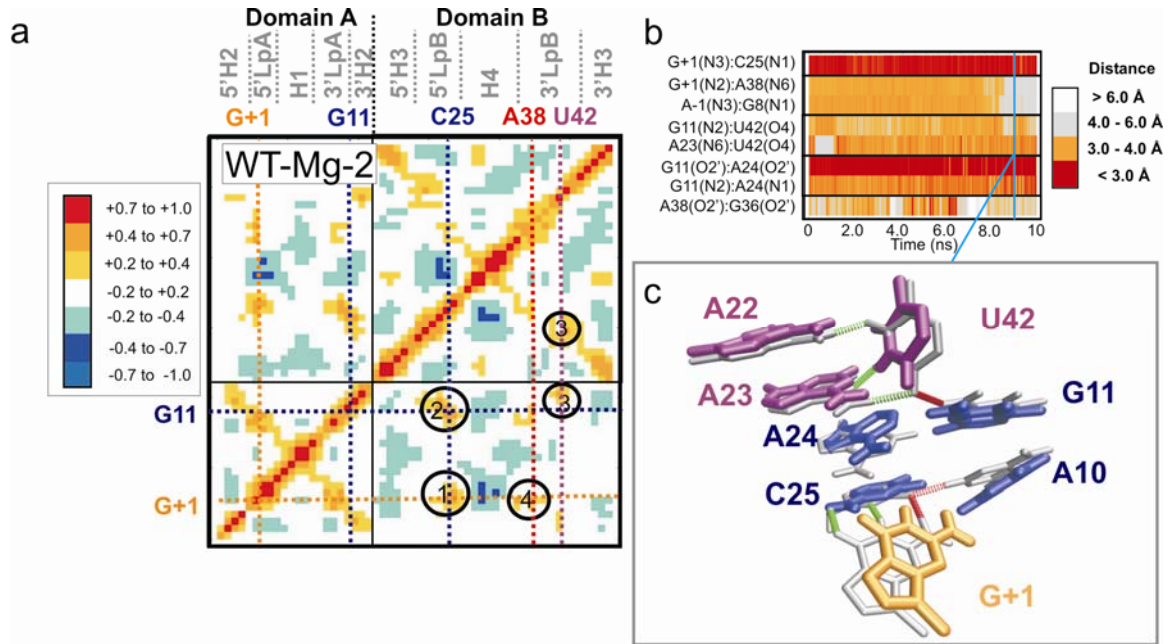
Rhodes et al., Figure 5



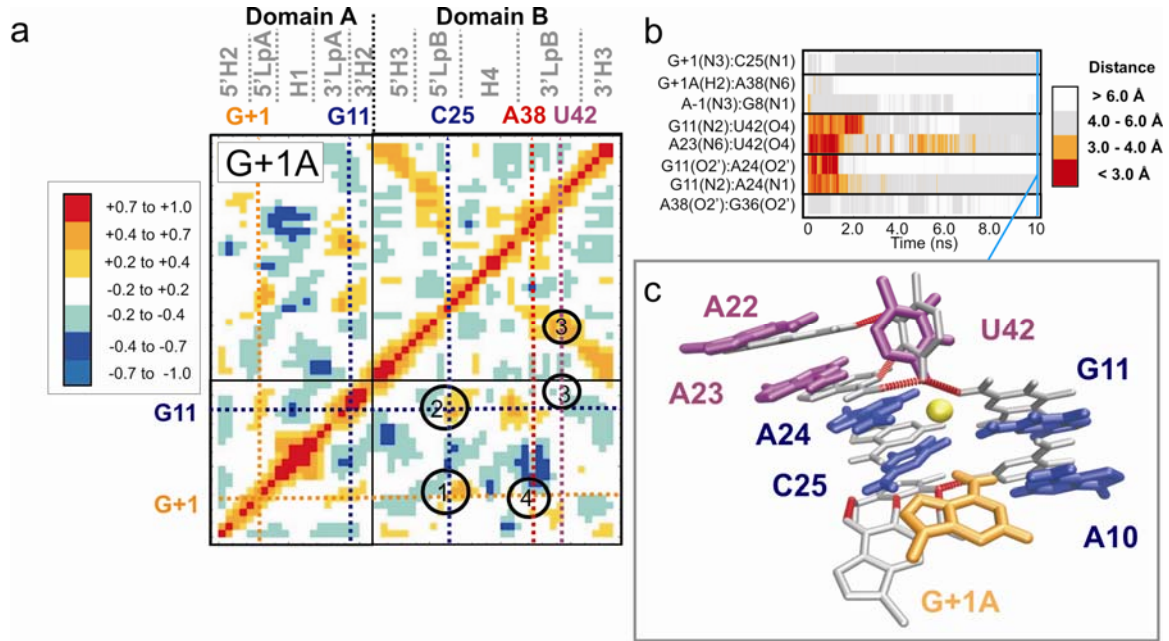
Rhodes et al., Figure 6



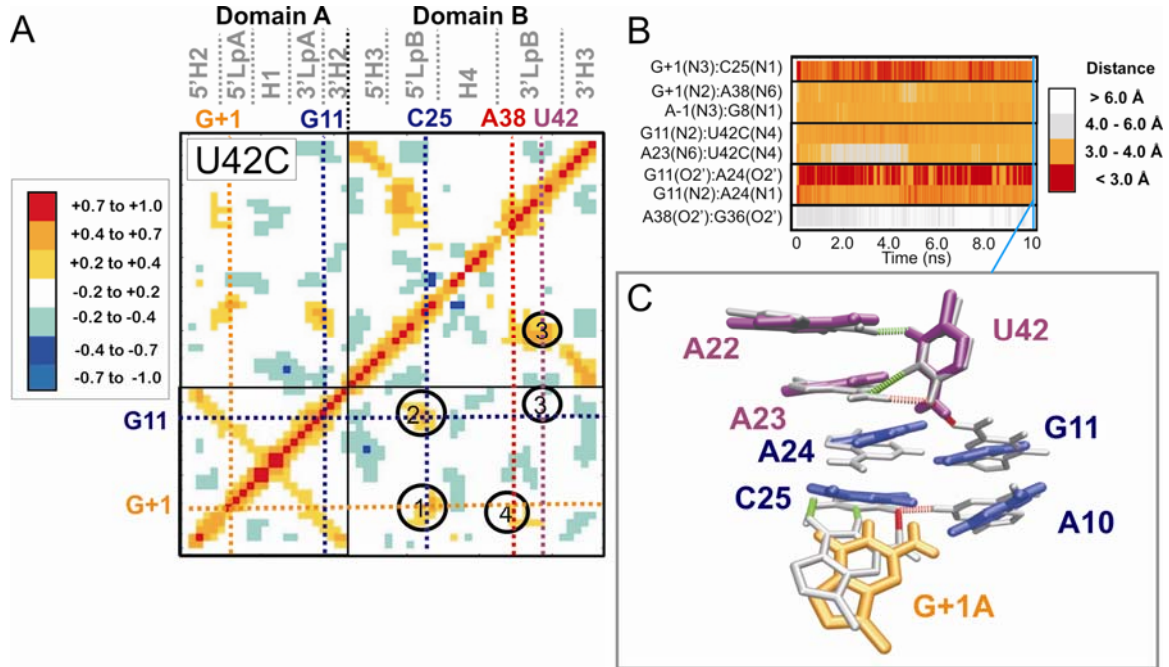
Rhodes et al., Figure 7



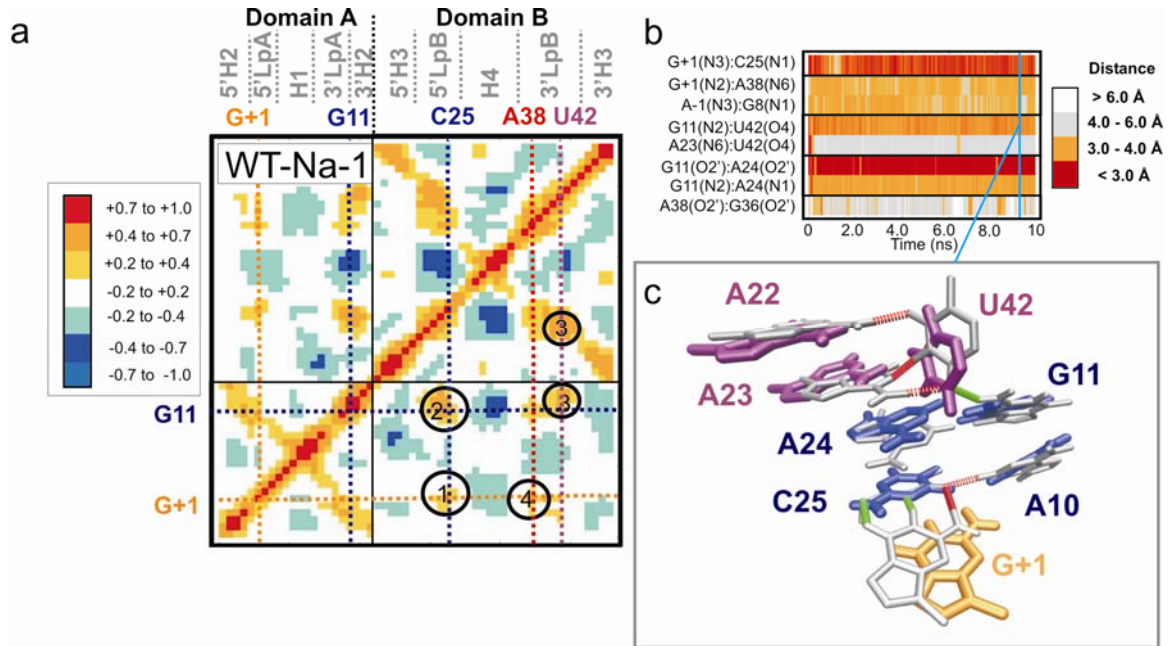
Rhodes et al., Figure 8



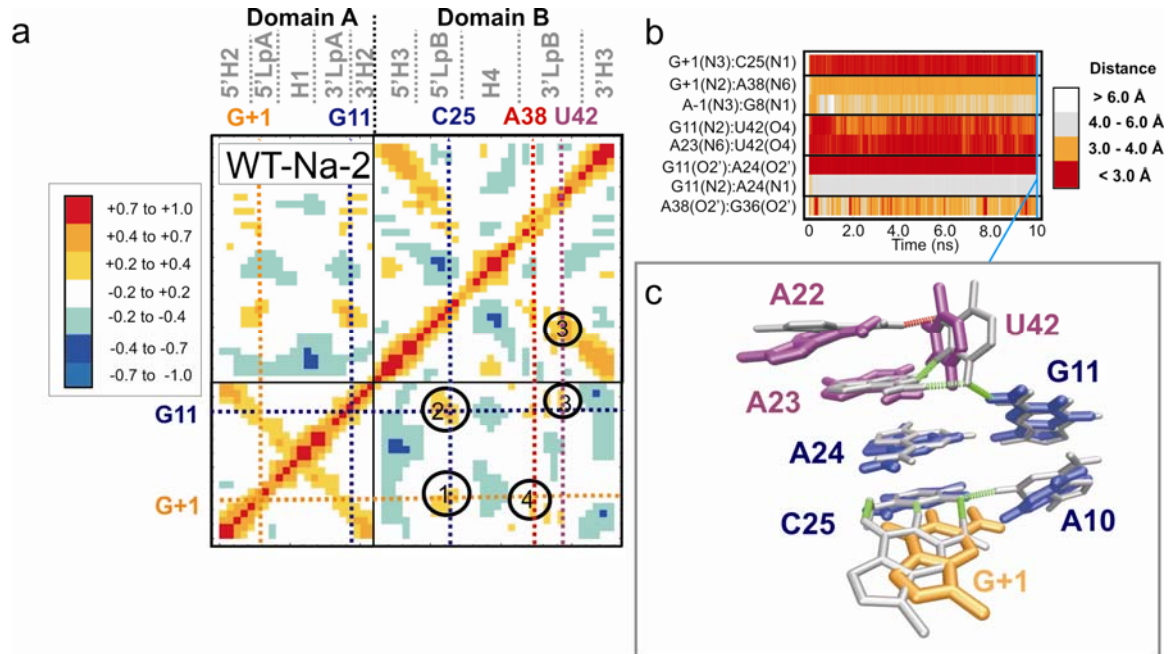
Rhodes et al., Figure 9



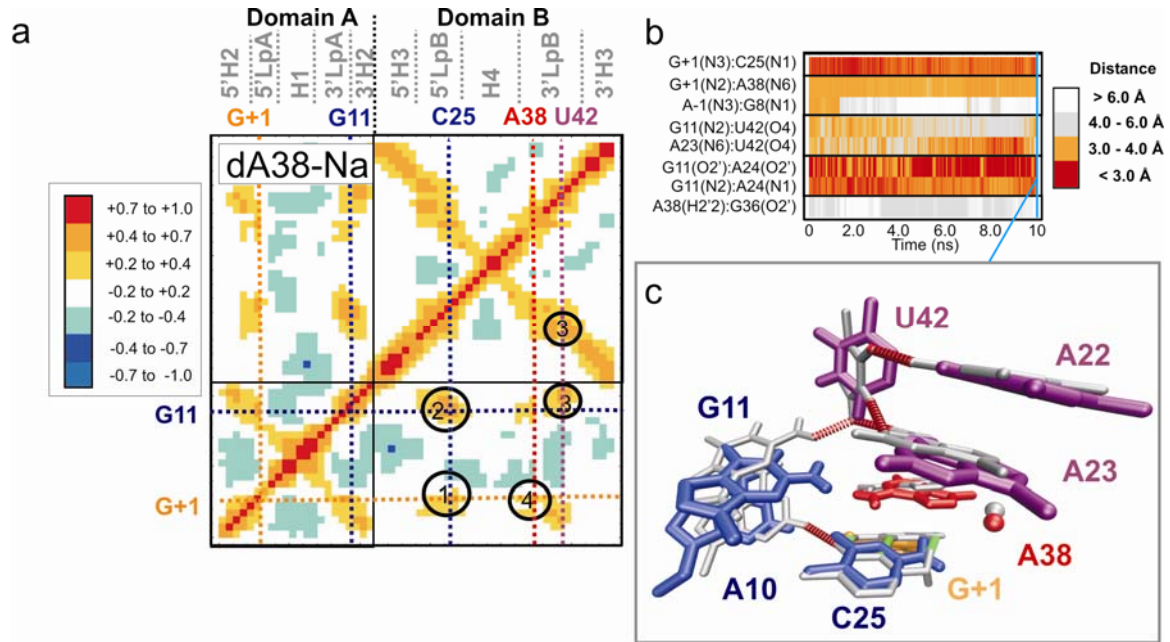
Rhodes et al., Figure 10



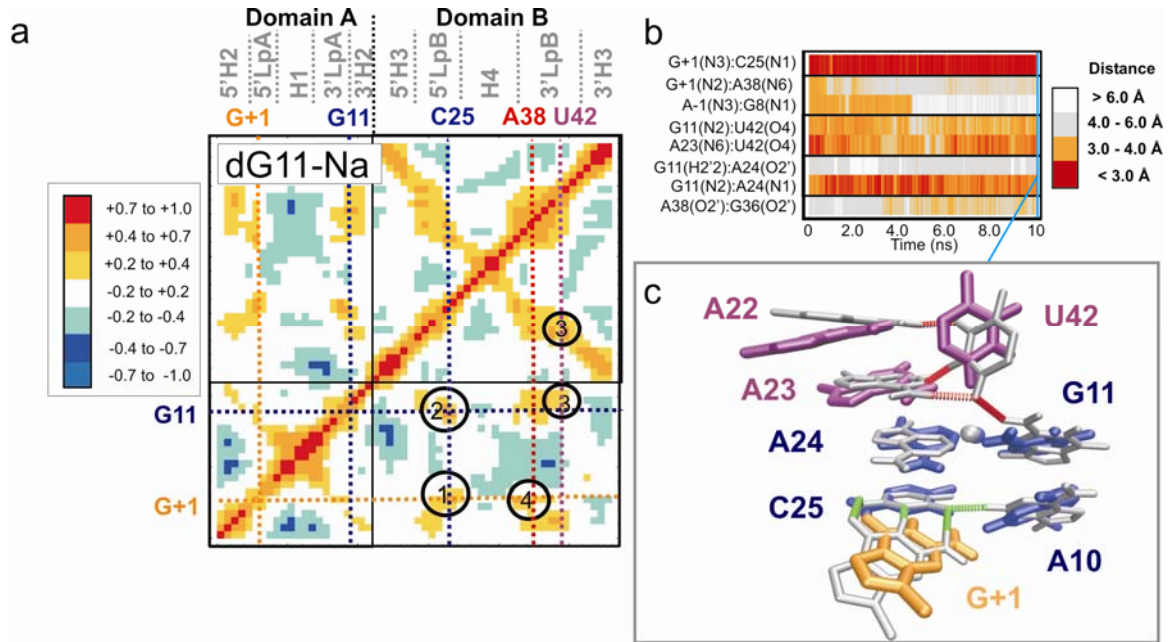
Rhodes et al., Figure 11



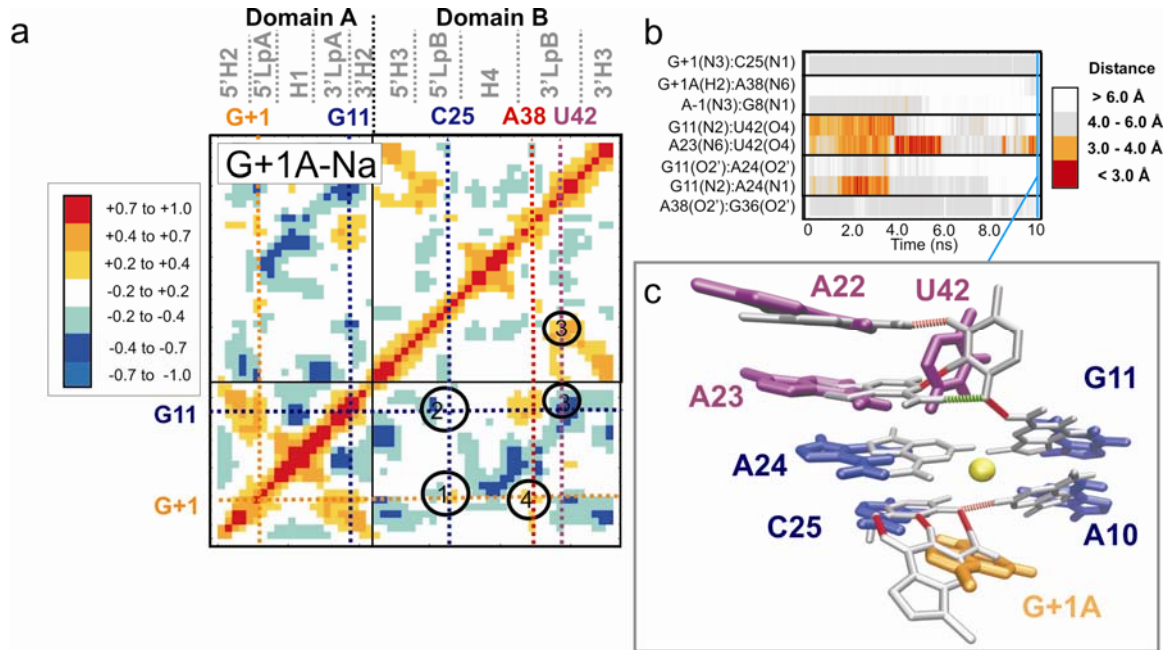
Rhodes et al., Figure 12



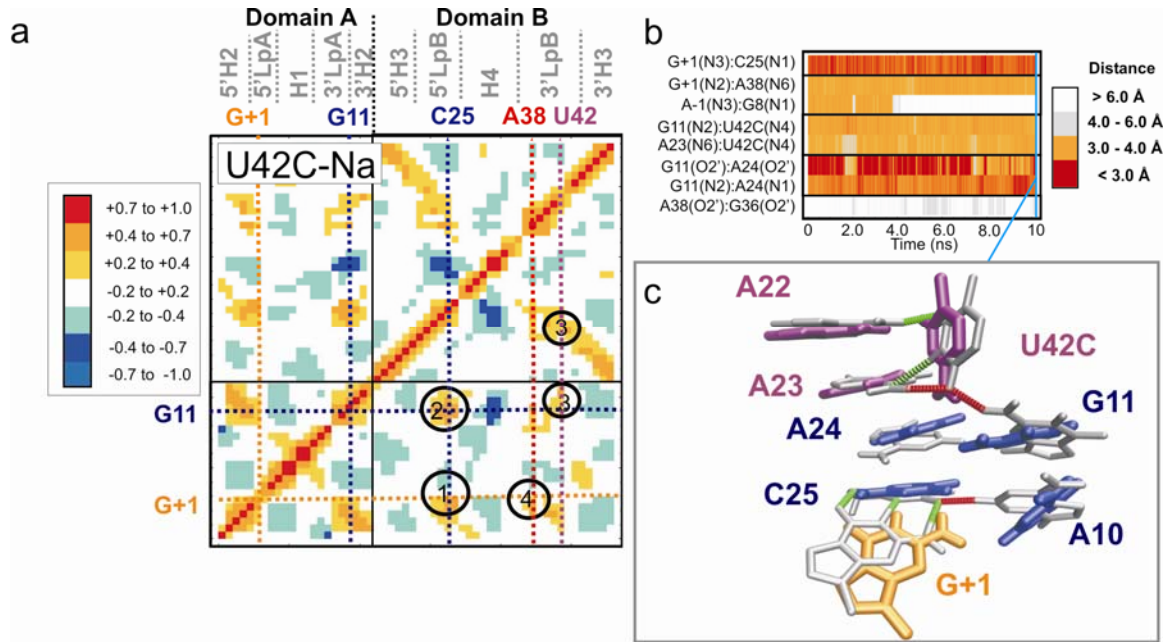
Rhodes et al., Figure 13



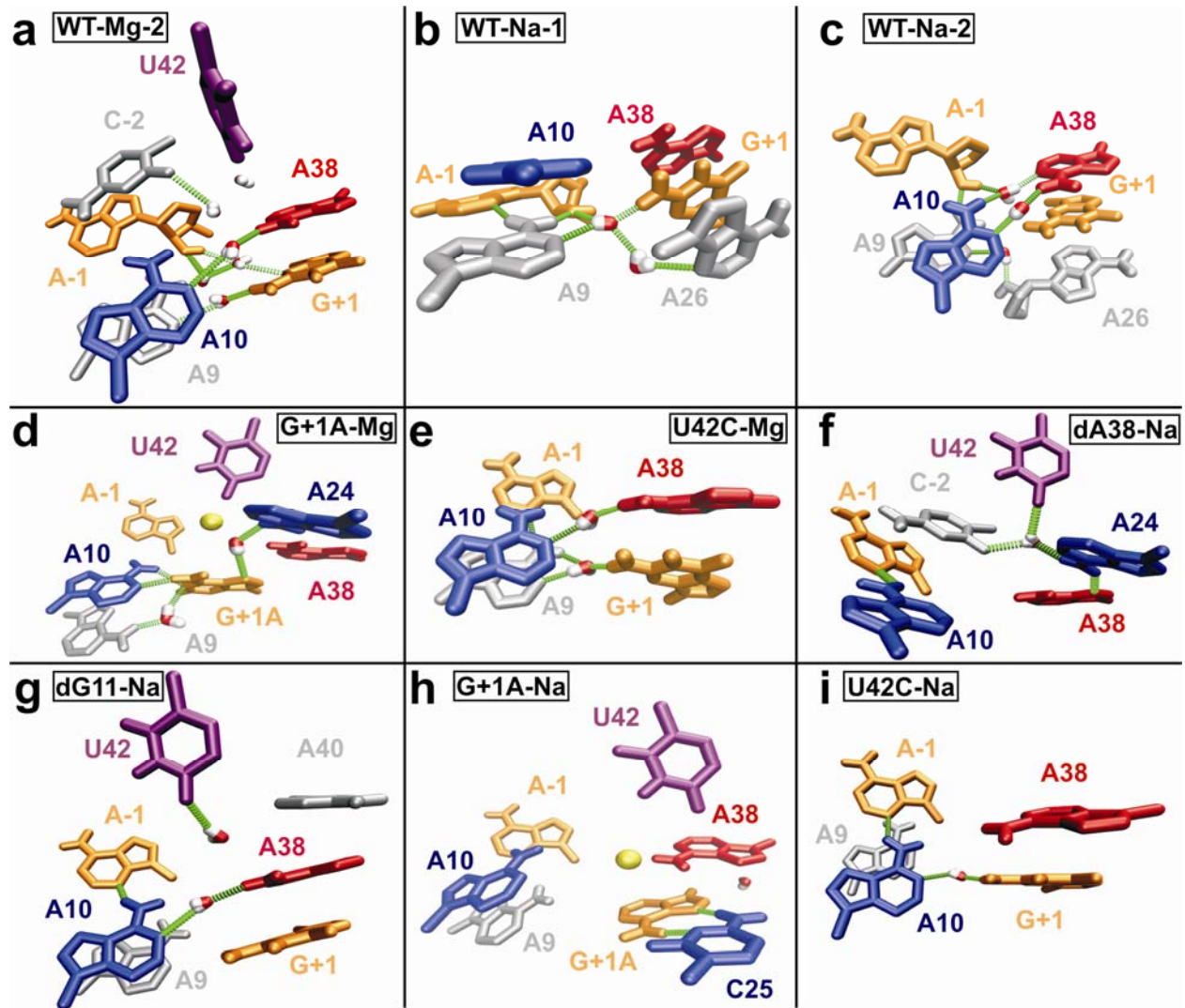
Rhodes et al., Figure 14



Rhodes et al., Figure 15



Rhodes et al., Figure 16



**Simulation WT-Mg-1
water residencies within
the catalytic core**

- A) 0.14 - 4.2 ns
- B) 0.40 - 4.9 ns
- C) 0.42 - 11.4 ns
- D) 0.58 ns - end
- E) 1.06 ns - end
- F) 1.10 ns - end
- G) 3.74 ns - end
- H) 4.04 - 19.3 ns
- I) 4.83 - 16.75 ns
- J) 17.66 ns - end

